



**HAL**  
open science

# Parameter identification of nonlinear time-dependent rubber bushings models towards their integration in multibody simulations of a vehicle chassis

Guillaume Puel, Béatrice Bourgeteau, Denis Aubry

## ► To cite this version:

Guillaume Puel, Béatrice Bourgeteau, Denis Aubry. Parameter identification of nonlinear time-dependent rubber bushings models towards their integration in multibody simulations of a vehicle chassis. *Mechanical Systems and Signal Processing*, 2013, 36 (2), pp.354-369. 10.1016/j.ymssp.2012.10.021 . hal-00799243

**HAL Id: hal-00799243**

**<https://centralesupelec.hal.science/hal-00799243>**

Submitted on 11 Mar 2013

**HAL** is a multi-disciplinary open access archive for the deposit and dissemination of scientific research documents, whether they are published or not. The documents may come from teaching and research institutions in France or abroad, or from public or private research centers.

L'archive ouverte pluridisciplinaire **HAL**, est destinée au dépôt et à la diffusion de documents scientifiques de niveau recherche, publiés ou non, émanant des établissements d'enseignement et de recherche français ou étrangers, des laboratoires publics ou privés.

# Parameter identification of nonlinear time-dependent rubber bushings models towards their integration in multibody simulations of a vehicle chassis

Guillaume Puel<sup>1</sup>, Béatrice Bourgeteau, Denis Aubry

*Laboratoire MSSMat, Ecole Centrale Paris / CNRS UMR 8579, Grande Voie des Vignes, 92290 Châtenay-Malabry, France*

---

## Abstract

Rubber bushings are extensively-used linking parts in a vehicle chassis that allow to filter noise and vibration. They influence much, however, the transient behaviour of the vehicle, such as its steering performance. Therefore building a multibody simulation with a relevant description of the rubber bushings is useful to describe the significant characteristics of the vehicle's steering behaviour. First, a nonlinear time-dependent model describing a rubber bushing's mechanical behaviour is presented. In order to be relevant, the parameters associated with this model are then identified from experimental tests using an adjoint state formulation of the identification problem. The identified values are eventually validated using additional experimental data.

*Keywords:* rubber bushings, nonlinear time-dependent model, parameter identification, adjoint state, multibody simulation

---

## 1. Introduction

2 Rubber bushings are mechanical parts that are extensively used to reduce  
3 noise and vibration in a vehicle chassis. They have, however, a strong im-  
4 pact on the whole vehicle chassis behaviour, such as its steering performance.

---

*Email addresses:* [guillaume.puel@ecp.fr](mailto:guillaume.puel@ecp.fr) (Guillaume Puel),  
[beatrice.bourgeteau@sagem.com](mailto:beatrice.bourgeteau@sagem.com) (Béatrice Bourgeteau), [denis.aubry@ecp.fr](mailto:denis.aubry@ecp.fr) (Denis Aubry)

<sup>1</sup>Corresponding author.

5 Since it is not always possible to get experimental data directly on the whole  
6 chassis system, their impact has to be described using a multibody simula-  
7 tion. This would include a relevant model of the rubber bushings mounted in  
8 the chassis. This paper focuses on the identification procedure that allows to  
9 determine the parameters associated with such a model. This will be done by  
10 means of experimental data derived from specific measurements on bushings  
11 mounted in test rigs.

12 The following provides an outline of the paper. First, the rubber bush-  
13 ings' behaviour enlightening the different phenomena to take into account  
14 in the model is briefly presented. Then the characteristics of the chosen  
15 model are given; two points are underlined: how relevant this choice is to  
16 describe the observed phenomena, and how the results coming from the as-  
17 sociated multibody simulations allow to describe some qualitative, but sig-  
18 nificant characteristics of the vehicle's steering behaviour. In order to derive  
19 more accurate, quantitative results from these simulations, the characteri-  
20 zation of the actual rubber bushings' behaviour is needed. Consequently, a  
21 series of measurements on test rigs have been performed in conjunction with  
22 several suppliers of bushings. These tests are primarily used as an experimen-  
23 tal reference in the identification procedure. This is the core of the study,  
24 which is described in detail: a misfit function expressing the discrepancy  
25 between the model's results and the experimental data is defined and then  
26 minimized by means of a gradient-based minimization algorithm using an  
27 adjoint state formulation. The identification results are eventually presented  
28 and discussed.

## 29 **2. Mechanical behaviour of the rubber bushings**

### 30 *2.1. Description of the mechanical part*

31 Rubber bushings are cylindrical parts that consist of a metallic inner core  
32 and a plastic or metallic outer frame linked one to the other by a rubber  
33 intermediate body (Figure 1). The inner core and the outer frames are  
34 connected to different parts of the chassis.

35 The geometry of the rubber intermediate body is not exactly axisym-  
36 metric: pits and ribs allow distinct behaviours for different load directions.  
37 Thus the bushing's tridimensional mechanical behaviour can be split into  
38 several simple uniaxial behaviours, corresponding to classical types of loads  
39 (axial, radial, torsional, ...). These different behaviours can be described in  
40 a simple way, for they can be directly related to the material behaviour of



Figure 1: Typical rubber bushing

41 rubber. Thus in the following, the study of the mechanical characteristics  
42 of rubber will be studied rather than the influence of the geometry of the  
43 rubber intermediate body.

#### 44 *2.2. Material mechanical behaviour of rubber*

45 Rubber usually exhibits three canonical components in its mechanical  
46 behaviour: an elastic component, which is totally reversible, and two dissi-  
47 pating (thus irreversible) components, which are hysteresis and viscoelastic-  
48 ity. Additional specific effects also have to be taken into account. All these  
49 behaviours have been listed in numerous references [1, 2, 3], which tried to  
50 propose some associated simple models as the basis of more complex models.

51 The elastic component is characterized by a nonlinear stress versus strain  
52 curve, which can be obtained from cyclic measurements involving high-amplitude  
53 displacements at low speed: in this case, the irreversible effects can be ne-  
54 glected. If not, one way to derive the stress versus strain curve is to flatten  
55 the obtained cycle into an average curve assumed to represent the elastic  
56 component only. Furthermore, for rather small displacements, as it is gener-  
57 ally the case for the bushings typically used, the stress versus strain relation  
58 can be considered as linear, or, at worst, as piecewise linear.

59 The hysteretic component is mainly due to the presence of carbon black  
60 as a reinforcing filler in rubber: inner friction-like phenomena due to these

61 particles create a history effect, which depends on the loading speed. This  
62 component is of utter importance for the vehicle chassis behaviour, especially  
63 at small amplitudes where hysteresis is the most significant effect.

64 Carbon black particles also have an additional impact on the bushing's  
65 secant stiffness, called the Payne effect [4]. The secant stiffness is considered  
66 when plotting the force versus displacement curve as cyclic displacements  
67 are applied to the bushing, and is defined as the slope of the secant line  
68 joining the two extreme points of the obtained hysteresis cycle. For small  
69 displacement amplitudes, the Payne effect consists in a secant stiffness that  
70 decreases rapidly as the loading amplitude increases. This effect is significant  
71 enough to be taken into account in the bushings typically used: it can be  
72 seen in experimental measurements that the higher the proportion of carbon  
73 black fillers, the stronger this effect.

74 Whereas hysteresis is often a rate-independent phenomenon, viscoelasticity  
75 on the contrary depends on the loading speed, and can be related to the  
76 friction that takes place between the rubber macromolecules. The associated  
77 effects are particularly significant in relaxation, which occurs when a displace-  
78 ment characterised by a Heaviside step function is applied to the bushing:  
79 the force versus time curve depends on the amplitude of the displacement  
80 step function as well as its speed (for the application of the displacement is  
81 not truly discontinuous). Relaxation has to be taken into account because it  
82 denotes an evanescent memory effect, which is crucial in the vehicle's steer-  
83 ing behaviour: two successive steering wheel rotations will not have the same  
84 effect depending if they are in the same direction or in opposite directions.

85 Another significant impact of the viscoelastic component can be observed  
86 in the frequency domain: there is a dynamic stiffening of the bushing as the  
87 loading frequency increases. The bushing's dynamic stiffness is derived from  
88 a first-harmonic analysis of the force obtained when a sinusoidal displacement  
89 is applied to the bushing: it is defined as the amplitude ratio of the force's  
90 (predominant) first harmonic to the displacement. This effect is opposed to  
91 the Payne effect: even if it is more limited, it should be taken into account  
92 in the bushing's model.

93 One last effect related to the mechanical behaviour of rubber should be  
94 evoked: the Mullins effect [5], which consists in a strong decrease in the  
95 bushing's secant stiffness occurring whenever the load increases beyond its  
96 prior all-time maximum value. After a few cycles at a given amplitude, it  
97 can then be assumed that the stiffness does not evolve any more, provided  
98 there is no applied load of higher amplitude. This damage-like effect, though

99 significant, will not be taken into account here, for it is assumed that all the  
100 bushings which are used in the chassis are first exerted in a burn-in process:  
101 they are submitted before operational service to various loads along different  
102 directions, so that the Mullins effect is no longer significant once the bushings  
103 have been mounted on the chassis.

### 104 **3. Mechanical model for the rubber bushings**

105 Since the typical geometry of a rubber bushing is designed such that  
106 the mechanical behaviours along the different directions are decoupled, the  
107 geometry influence is not further studied, and a simple model can be proposed  
108 for each loading mode. Furthermore, the model should be chosen as simple  
109 as possible so that its implementation in a multibody simulation software  
110 could be easy and robust. Therefore rheological models are used that have  
111 to represent the different components described in Section 2.2. The degrees  
112 of freedom (DOFs) associated with these models correspond to the nodes  
113 linking the different rheological components. They are the solutions of the  
114 Ordinary Differential Equations (ODEs) associated with the chosen models.

#### 115 *3.1. Standard Triboelastic Solid model (STS)*

116 The Standard Triboelastic Solid model (STS), initially proposed by Coveney [6]  
117 for seismic rubber bushings, is based on the linear superposition of a pure  
118 elastic behaviour (described by a spring element) and a hysteretic component  
119 (described by a solid friction element): the resulting combination, depicted  
120 in Figure 2, is the STS elementary cell, whose combination in series can rep-  
121 resent a typical hysteretic cycle, for the different friction elements allow to  
122 reproduce the desired memory effect. The parameters associated with the  
123 STS elementary cell are the stiffness  $K_r$  of the spring element and the thresh-  
124 old force  $F_f$  of the friction element, which means that the friction element  
125 slides if and only if the norm of the load acting on it is higher than the  
126 specified threshold  $F_f$ .

127 Eventually, the proposed STS model, shown in Figure 3, is based on the  
128 serial combination of several identical STS elementary cells, along with two  
129 additional springs,  $K_0$  and  $K_{pa}$ , standing for a global elastic stiffness and an  
130 additional stiffness for low-amplitude displacements respectively. The STS  
131 elementary cells are chosen identical for the sake of simplicity. Consequently,  
132 the proposed STS model is based on four distinct parameters, for the number

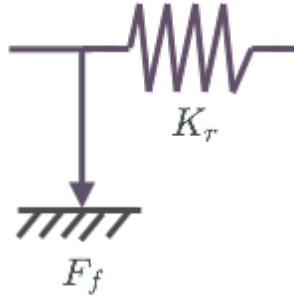


Figure 2: STS elementary cell

133 of STS elementary cells can generally be set once and for all. This number,  
 134 indeed, allows a more or less fine discretization of the hysteresis cycle.

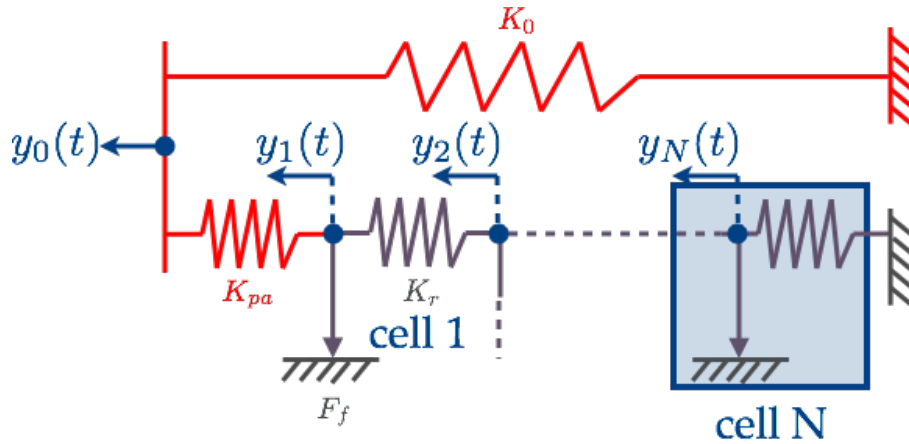


Figure 3: STS model with  $N$  identical STS elementary cells

135 Although the STS model is able to represent the hysteretic component  
 136 of the rubber bushing, it does not account for viscoelasticity. To take it into  
 137 account, most current models add in parallel to the STS model elements with  
 138 viscoelastic behaviour. For example, a Maxwell cell (*i.e.* viscous damping) is  
 139 added in parallel in [7], but it generally seems difficult to suit the bushing's  
 140 global dynamical response: [8] shows that using a viscous damping tends to  
 141 entail an overestimation of the efforts in play.

142 *3.2. Rate-dependent Triboelastic model (RT)*

143 Rather than add other components to the previous model, a better solu-  
 144 tion seems to replace the friction elements of the STS model by components  
 145 exhibiting a viscoelastic behaviour: this is the Rate-dependent Triboelas-  
 146 tic model (RT), proposed by Coveney as well [7]. The RT elementary cell  
 147 comprises a linear spring element with stiffness  $K_r$  and a nonlinear viscous  
 148 dashpot put in parallel. The force versus velocity law of the dashpot is  
 149 characterized by two parameters  $(C_0, \alpha)$  such that:

$$F_k(t) = C_0 \text{sign}(y'_k(t)) |y'_k(t)|^\alpha \quad (1)$$

150 where  $F_k(t)$  is the force applied on the dashpot and  $y'_k(t)$  is the velocity of  
 151 the corresponding DOF.  $\alpha$  is chosen such that  $0 < \alpha < 1$ : depending on this  
 152 value, the dashpot exhibits different behaviours. In particular, if  $\alpha = 0$ , the  
 153 dashpot is exactly equivalent to the solid friction element used in the STS  
 154 model (when  $C_0 = F_f$ ).

155 Eventually, the proposed RT model is based on the serial combination  
 156 of several identical RT elementary cells, along with two additional springs,  
 157  $K_0$  and  $K_{pa}$ , standing for a global elastic stiffness and an additional elastic  
 158 stiffness for low-amplitude displacements respectively. The RT elementary  
 159 cells are chosen identical again for the sake of simplicity, resulting in the  
 160 assembly depicted in Figure 4.

161 Since, once again, the number  $N$  of RT elementary cells is set a priori (al-  
 162 lowing a more or less fine discretization of the hysteretic cycle), the proposed  
 163 RT model depends on  $P = 5$  distinct parameters:  $\mathbf{p} = (K_0 \ K_{pa} \ K_r \ C_0 \ \alpha)^T$ .  
 164 The forward problem thus consists in solving the following system of  $N$  time-  
 165 dependent ODEs:

$$\begin{aligned} (K_{pa} + K_r)y_1(t) - K_r y_2(t) + C_0 \text{sign}(y'_1(t)) |y'_1(t)|^\alpha &= K_{pa} y_0(t) & (2) \\ \vdots & \\ -K_r y_{k-1}(t) + 2K_r y_k(t) - K_r y_{k+1}(t) + C_0 \text{sign}(y'_k(t)) |y'_k(t)|^\alpha &= 0 \\ \vdots & \\ -K_r y_{N-1}(t) + 2K_r y_N(t) + C_0 \text{sign}(y'_N(t)) |y'_N(t)|^\alpha &= 0 \end{aligned}$$

166 for  $1 < k < N$ . The different DOFs  $(y_k(t))_{1 \leq k \leq N}$  are the components of  
 167 the state vector  $\mathbf{y}(t)$ , whereas  $y_0(t)$  is the prescribed displacement. It is also  
 168 assumed that the initial conditions for each DOF are equal to zero.

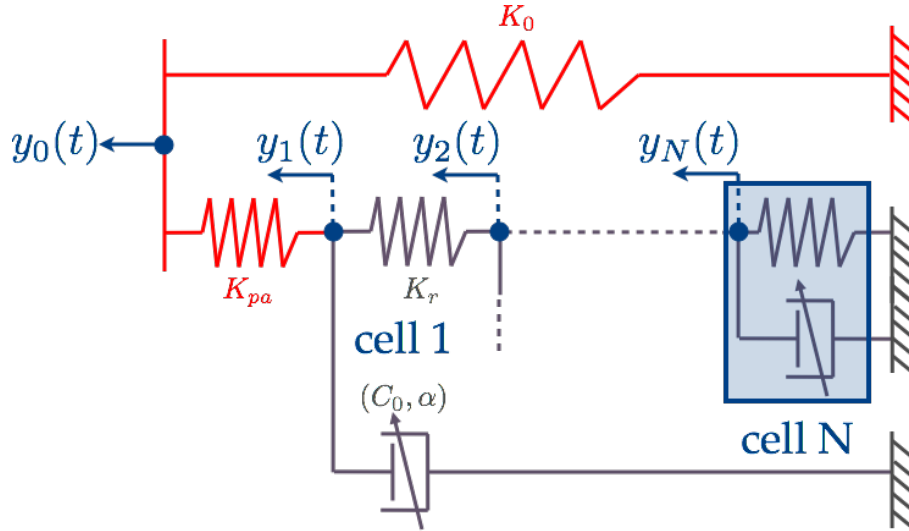


Figure 4: RT model with  $N$  identical RT elementary cells

169 *3.3. Other models*

170 In addition to these two previous models, numerous models relying on  
 171 alternative choices of rheological components have been proposed and exten-  
 172 sively studied. For example, a fractional derivative model can be introduced  
 173 in the viscoelastic part [9]. This kind of model, used in [10] along with a gen-  
 174 eralized friction force element, allows to accurately account for the evolutions  
 175 of the dynamic stiffness of rubber isolators as the frequency and amplitude  
 176 of the excitation, as well as the static precompression, evolve. This model,  
 177 however, seems hardly suited to be implemented in a multibody simula-  
 178 tion, because most of the associated algorithms used to solve the fractional  
 179 derivative part in the time domain are rather sophisticated [11], or can be  
 180 very time-consuming. Furthermore, the parameter identification seems far  
 181 more awkward in the time domain than in the frequency domain.

182 Another widely-used model coming from [12] then [13] is the Bouc-Wen  
 183 model consisting in a parametric hysteretic loop along with a spring and a  
 184 linear viscous dashpot in parallel. The identification of the parameters as-  
 185 sociated with this model has been achieved in [14] in the frequency domain  
 186 using a harmonic balance approximation. Used as is, however, the Bouc-Wen  
 187 model exhibits some inconsistencies when compared with experimental data,  
 188 and tends to overestimate the rate-independent hysteretic part relatively to

189 the rate-dependent part. Several modifications have been introduced to im-  
 190 prove the model, such as in [15] recently: the proposed model consists in  
 191 two simple Bouc-Wen models put in parallel along with a spring and a linear  
 192 viscous dashpot. Even if this modified Bouc-Wen model gives better predic-  
 193 tions of the bushing’s behaviour, it depends on 16 independent parameters.  
 194 This makes the parameter identification rather difficult: in [15], a genetic  
 195 algorithm is proposed, but the identified values of the different parameters  
 196 strongly depend on the experimental data used in the identification process,  
 197 because the inverse problem is significantly ill-posed due to the high number  
 198 of parameters. The authors then propose to combine several experimental  
 199 test results to improve the identification, but the process eventually seems  
 200 to be delicate to apply.

### 201 3.4. Simulations examples using the RT model

202 Considering the conclusions of the previous section, the RT model seems  
 203 to be the most relevant choice. First the number of RT cells has to be set  
 204 so that the predictions are sufficiently refined to be similar to the curves  
 205 obtained with the available measurements. Typically  $N$  can be directly re-  
 206 lated to the discretization of hysteresis cycles as far as the simulation of  
 207 quasistatic periodic displacements is concerned: Figure 5 shows the hys-  
 208 teresis cycles obtained for different values of  $N$ . The different parameters  
 209  $\{K_0, K_{pa}, K_r, C_0, \alpha\}$  have been chosen such that the simulated cycles have  
 210 similar features, *i.e.* the same values of the maximum load, the secant stiff-  
 211 ness, and the tangents before and after cusps. For  $N \geq 10$ , the obtained  
 212 curves have converged to a limit cycle whose smoothness seems satisfactory.  
 213 Finally,  $N = 15$  cells are chosen to be able to account for applied displace-  
 214 ments which would be larger than the ones proposed in the measurements,  
 215 which could possibly happen in the vehicle chassis in operation.

216 In Figure 6, different simulations using the proposed RT model with  
 217  $N = 15$  elementary cells are depicted and show the model’s ability to grasp  
 218 most of the effects described in Section 2.2. On the left of Figure 6, the  
 219 force-displacement curves, obtained when sinusoidal displacements are ap-  
 220 plied to the bushing, are plotted: they clearly show the bushing’s stiffening as  
 221 the loading frequency increases. More precisely, the secant stiffness, defined  
 222 as the ratio between the maximum load and the maximum displacement,  
 223 increases by 4% between 1Hz and 10Hz, and by 4.5% between 10Hz and  
 224 100Hz. On the right of Figure 6, one shows the force obtained when a dis-  
 225 placement described by a Heaviside step function is applied to the bushing:

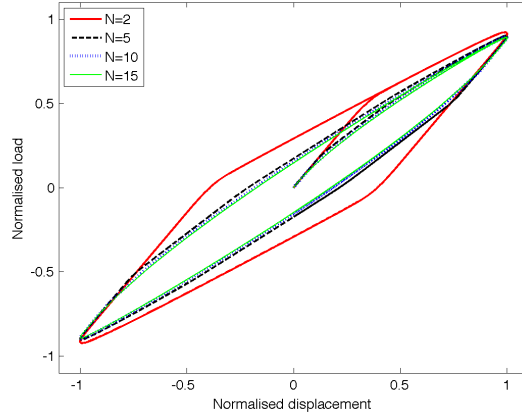


Figure 5: Numerical simulations obtained with the RT model for different numbers of cells

226 relaxation is clearly observed, until the force goes down to a given constant  
 227 value, consistent with the bushing's static behaviour and the value of the  
 228 applied steady-state displacement. In the same way, it is possible to verify  
 229 that the proposed RT model is able to account for the Payne effect as well.

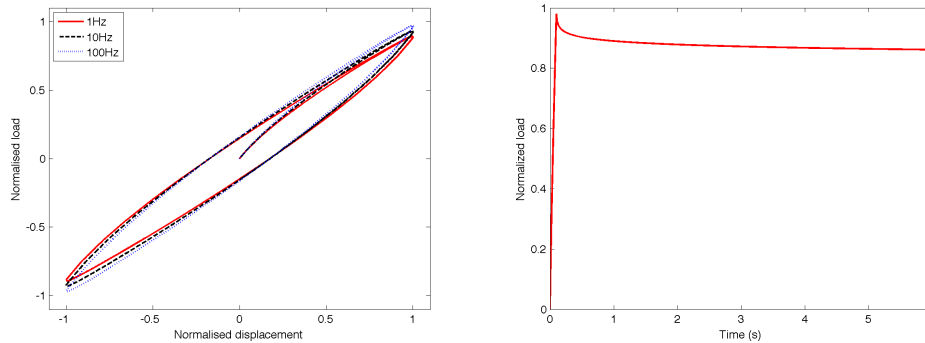


Figure 6: Numerical simulations obtained with the RT model for different prescribed displacements: sines of increasing frequencies (left) and Heaviside step function (right)

### 230 3.5. Implementation in a multibody simulation code

231 The RT model has then been implemented in a multibody simulation  
 232 of a typical chassis using ADAMS software. More precisely, user functions

233 programmed in Fortran allow to compute the load associated with the chosen  
234 model when a given displacement is applied to the rubber bushing.

235 Two different strategies are available. Using a GSESUB user function  
236 allows to solve the ODEs associated with the RT model along with the re-  
237 maining equations associated with the whole multibody system. On the  
238 contrary, when a VARSUB user function is used, one has to implement di-  
239 rectly in the subroutine the time integration algorithm. These two strategies  
240 have been tested on the very simple model of a beam linked to the ground  
241 by a rubber bushing whose mechanical behaviour is described by the RT  
242 model. They lead to similar results in terms of simulation results and ac-  
243 curacy. Nevertheless the VARSUB function seems to have more advantages  
244 than the GSESUB function: it is possible to implement any time integration  
245 scheme, independently from the one used for the remaining elements of the  
246 structure, and the computation time tends to be shorter. The final choice  
247 has then consisted of an explicit Euler scheme defined in the VARSUB func-  
248 tion. The time step is chosen accordingly to the variable time step used by  
249 ADAMS, by dividing this latter by a given factor, which allows to guarantee  
250 the stability of the Euler time integration scheme.

251 Different simulations have been run on a complete multibody model of a  
252 typical small family car using RT models for the rubber bushings mounted  
253 in the front and rear axles of the vehicle. Only two specific results are shown  
254 here, and are associated with one specific rubber bushing, mounted in the  
255 rear axle, as depicted in Figure 7. This rubber bushing, which links the  
256 rear crossbeam to the body, allows to filter vertical vibrations as well as to  
257 transmit longitudinal forces to the axle.

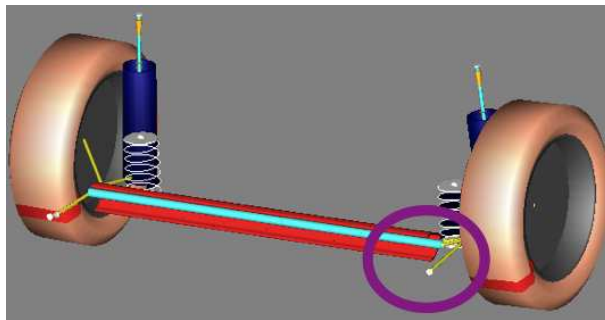


Figure 7: Location of one specific rubber bushing in the rear axle (partial view of the multibody model of a typical small family car)

258 A first simulation focuses on how the studied bushing behaves when an  
 259 angle characterised by a Heaviside step function is applied to the steering  
 260 wheel of the vehicle (actually, the angular input is not truly discontinuous,  
 261 but is characterised by a short time interval of constant angular velocity).  
 262 Figure 8 shows the radial horizontal load in the bushing with respect to time  
 263 in two different cases, depending on whether a RT model or a STS model  
 264 is used to describe the rubber bushing's behaviour. The two curves are  
 265 normalised by the respective maximum load values, which allows to easily  
 266 compare the two models. This comparison stresses the lack of relaxation  
 267 when using the STS model, whereas the RT model is able to account for this  
 268 effect, as expected.

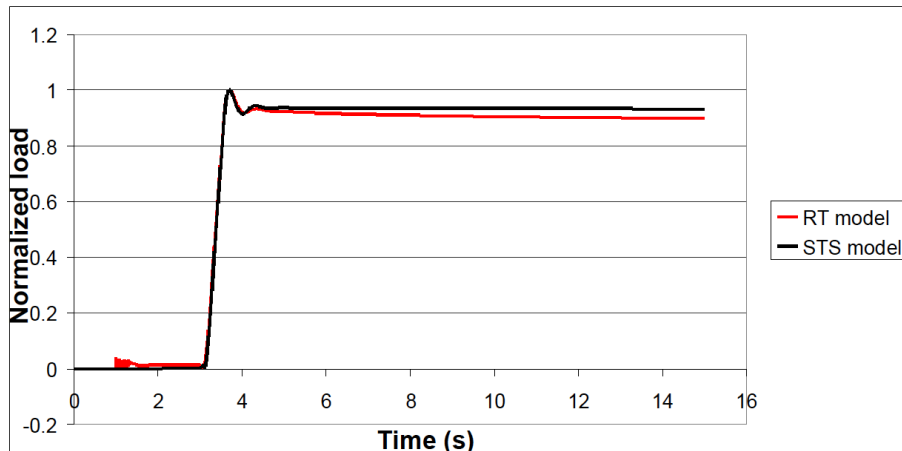


Figure 8: Normalised load in the bushing with respect to time (angular Heaviside step function on the steering wheel): RT model (red) and STS model (black)

269 A second simulation allows to represent well-known phenomena in the  
 270 steering behaviour such as the evanescent memory effect. On the right of  
 271 Figure 9 the (normalised) load acting on the studied bushing is shown, when  
 272 two successive rotations (each described by a Heaviside step function) are  
 273 applied to the vehicle's steering wheel. This kind of input is inspired from  
 274 classical elk tests, consisting in avoiding an obstacle without braking and then  
 275 coming back to the right lane. Depending on whether these two rotations  
 276 are of the same direction or occur in opposite ways (as formally depicted on  
 277 the left of Figure 9), the load acting on the bushing can be very different:  
 278 the relaxation effect is stronger in the second case. This has an impact

279 on the toe and camber angles of the wheel associated with the bushing of  
 280 interest. Similar results can be obtained for other bushings, allowing to  
 281 conclude on the impact on the vehicle's steering behaviour, which is a well-  
 282 known phenomenon described by test drivers.

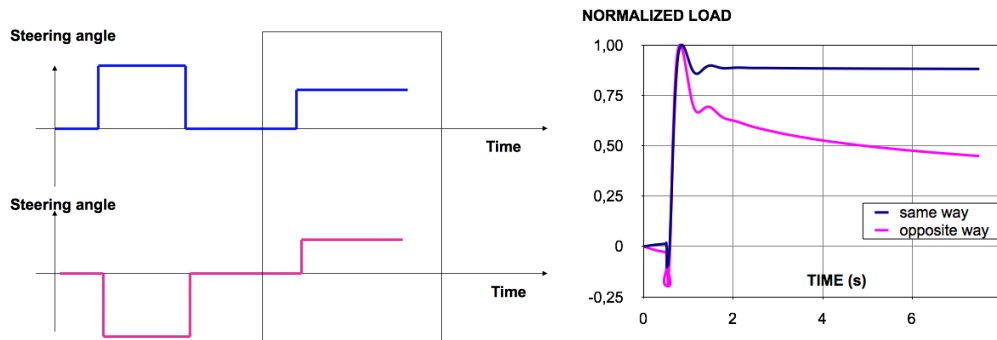


Figure 9: Normalised load during the second of two successive rotations of the vehicle's steering wheel: (blue) rotations of the same direction (pink) rotations of opposite directions (a positive rotation is equivalent to a left turn of the steering wheel)

283 The previous examples then demonstrate the relevance of the results pre-  
 284 dicted by the multibody simulation. However, without experimental data,  
 285 which would be directly measured on the whole vehicle on the track, these  
 286 predictions remain essentially qualitative. In order to turn these results into  
 287 quantitative predictions, the next step consists in finding the correct values  
 288 for the RT model's parameters. Since experimental information is available  
 289 for each rubber bushing (coming from specific measurements in test rigs), the  
 290 values of these parameters should be identified so that the response of a bush-  
 291 ing, which is calculated using the RT model under a given loading mode, fits  
 292 best the experimental measurements obtained with the same loading mode.

#### 293 4. Generic formulation of the identification problem

294 For the sake of clarity, the identification problem as it is defined and  
 295 solved is first presented in a generic way. The parameter identification of the  
 296 RT model of rubber bushings is developed in the next section.

297 *4.1. Generic formulation of the identification problem*

298 The forward problem (2) associated with the RT model can be described  
 299 by the following implicit vector formulation of size  $N$ :

$$\begin{aligned} \mathcal{F}(\mathbf{y}(t), \mathbf{y}'(t), \mathbf{p}, t) &= \mathbf{0} \quad \forall t \in [0, T] \\ \mathbf{y}(0) &= \mathbf{0} \end{aligned} \quad (3)$$

300 where  $\mathbf{p}$  of size  $P$  and  $\mathbf{y}$  of size  $N$  are, just as before, the parameter vector and  
 301 the state vector comprising all the DOFs of the forward model respectively.

302 For the identification problem, it can then be assumed that the exper-  
 303 imental data will be compared with quantities derived from the different  
 304 DOFs of the forward problem by means of a projection operator denoted  $\mathbf{A}$ ,  
 305 of size  $n \times N$ , where  $n$  is the number of experimental measurements. Simi-  
 306 larly, it is assumed that the experimental data can be written as if they were  
 307 derived from an experimental state vector of size  $N$ : this assumption has no  
 308 other consequence than allowing a clearer presentation of the identification  
 309 problem. Eventually, a so-called misfit function is defined, which expresses  
 310 the discrepancy between the  $n$  measurements  $\mathbf{A}\mathbf{y}_{exp}(t)$  and the  $n$  associated  
 311 quantities derived from the model  $\mathbf{A}\mathbf{y}(t; \mathbf{p})$ :

$$\mathcal{J}(\mathbf{p}) = \frac{1}{2} \int_0^T |\mathbf{A}(\mathbf{y}(t; \mathbf{p}) - \mathbf{y}_{exp}(t))|^2 dt + \frac{1}{2} |\mathbf{R}(\mathbf{p} - \mathbf{p}_0)|^2 \quad (4)$$

312 where  $\mathbf{y}(t; \mathbf{p})$  is the solution of the state equation (3) calculated with param-  
 313 eters  $\mathbf{p}$ . Since the forward problem is nonlinear, it seems relevant to use a  
 314 time formulation of the misfit function, hence the integral over time.

315 The last term of the misfit function is a norm introduced to regularize the  
 316 inverse problem, by expressing that the sought parameters  $\mathbf{p}$  should be close  
 317 to a vector  $\mathbf{p}_0$  of typical values, with  $\mathbf{R}$  a diagonal operator whose values are  
 318 to be set. This so-called Tikhonov's regularization term aims at reducing the  
 319 ill-posedness of the identification process by bounding the magnitude of the  
 320 sought parameters.

321 *4.2. Minimization of the misfit function*

322 The identification problem consists in minimizing the misfit function (4)  
 323 to find the parameters allowing the model to be as close to the experimen-  
 324 tal data as possible. This minimization is usually performed by means of  
 325 gradient-based techniques, where the derivative of  $\mathcal{J}(\mathbf{p})$  is analytically intro-  
 326 duced using an adjoint state problem. This method was described in [16],

327 which deals with the identification of elastoplastic constitutive laws, whose  
 328 form is quite similar to the kind of law used in the RT model.

329 The solution  $\mathbf{z}(t)$  of this adjoint state problem can be considered as a La-  
 330 grange multiplier introduced in the following Lagrangian function  $\mathcal{L}(\mathbf{y}, \mathbf{p}, \mathbf{z})$ :

$$\begin{aligned} \mathcal{L}(\mathbf{y}, \mathbf{p}, \mathbf{z}) = & \frac{1}{2} \int_0^T |\mathbf{A}(\mathbf{y}(t) - \mathbf{y}_{exp}(t))|^2 dt + \frac{1}{2} |\mathbf{R}(\mathbf{p} - \mathbf{p}_0)|^2 \quad (5) \\ & - \int_0^T \mathcal{F}(\mathbf{y}(t), \mathbf{y}'(t), \mathbf{p}, t)^T \mathbf{z}(t) dt - \mathbf{y}(0)^T \mathbf{z}(0) \end{aligned}$$

331 where  $(\mathbf{y}, \mathbf{p}, \mathbf{z})$  are considered independent and  $(\cdot)^T$  is the transposition. Min-  
 332 imizing the misfit function  $\mathcal{J}(\mathbf{p})$  where  $\mathbf{y}$  verifies (3) is then equivalent to  
 333 writing the first-order stationarity conditions for  $\mathcal{L}(\mathbf{y}, \mathbf{p}, \mathbf{z})$ . This can be  
 334 clearly seen when expressing the first-order stationarity condition with re-  
 335 spect to  $\mathbf{z}$ :

$$- \int_0^T \mathcal{F}(\mathbf{y}(t), \mathbf{y}'(t), \mathbf{p}, t)^T \delta \mathbf{z}(t) dt - \mathbf{y}(0)^T \delta \mathbf{z}(0) = 0 \quad (6)$$

336 for any admissible  $\delta \mathbf{z}(t)$ . This expression is actually the weak formulation of  
 337 the state equation (3).

#### 338 4.3. Adjoint state problem

339 When writing the first-order stationarity condition for  $\mathcal{L}(\mathbf{y}, \mathbf{p}, \mathbf{z})$  with  
 340 respect to  $\mathbf{y}$ , the following relation is obtained:

$$\begin{aligned} & \int_0^T \delta \mathbf{y}(t)^T \left( \mathbf{A}^T \mathbf{A}(\mathbf{y}(t) - \mathbf{y}_{exp}(t)) \right) dt \quad (7) \\ & - \int_0^T \left( \nabla_{\mathbf{y}} \mathcal{F} \delta \mathbf{y}(t) + \nabla_{\mathbf{y}'} \mathcal{F} \delta \mathbf{y}'(t) \right)^T \mathbf{z}(t) dt - \delta \mathbf{y}(0)^T \mathbf{z}(0) = 0 \end{aligned}$$

341 for any  $\delta \mathbf{y}(t)$  verifying null initial conditions.  $\nabla_{\mathbf{y}} \mathcal{F}$  and  $\nabla_{\mathbf{y}'} \mathcal{F}$  stand for the  
 342 directional derivatives of  $\mathcal{F}$  with respect to  $\mathbf{y}$  and  $\mathbf{y}'$  respectively. After  
 343 integrating by parts, the previous weak formulation leads to the following  
 344 expression:

$$\begin{aligned} & \int_0^T \delta \mathbf{y}(t)^T \left( \mathbf{A}^T \mathbf{A}(\mathbf{y}(t) - \mathbf{y}_{exp}(t)) \right) dt \quad (8) \\ & - \int_0^T \delta \mathbf{y}(t)^T \left( \nabla_{\mathbf{y}} \mathcal{F}^T \mathbf{z}(t) - (\nabla_{\mathbf{y}'} \mathcal{F}^T \mathbf{z}(t))' \right) dt - \delta \mathbf{y}(T)^T \nabla_{\mathbf{y}'} \mathcal{F}^T \mathbf{z}(T) = 0 \end{aligned}$$

345 which is equivalent to the following strong formulation defining the adjoint  
 346 state problem:

$$\begin{aligned} \nabla_{\mathbf{y}} \mathcal{F}^T \mathbf{z}(t) - (\nabla_{\mathbf{y}'} \mathcal{F}^T \mathbf{z}(t))' &= \mathbf{A}^T \mathbf{A}(\mathbf{y}(t) - \mathbf{y}_{exp}(t)) \quad \forall t \in [0, T] \quad (9) \\ \nabla_{\mathbf{y}'} \mathcal{F}^T \mathbf{z}(T) &= \mathbf{0} \end{aligned}$$

347 The adjoint state problem is classical [16] and consists in solving for  $\mathbf{z}(t)$  a  
 348 linear time-backward ODE along with final conditions.

#### 349 4.4. *Optimality conditions for the parameters*

350 Once the adjoint state problem is solved, the gradient of the misfit func-  
 351 tion with respect to  $\mathbf{p}$  can be evaluated. Because of the equivalence between  
 352 the constrained minimization of  $\mathcal{J}(\mathbf{p})$  and the stationarity of  $\mathcal{L}(\mathbf{y}(t; \mathbf{p}), \mathbf{p}, \mathbf{z}(t))$ ,  
 353 it can be written that:

$$\nabla_{\mathbf{p}} \mathcal{J}(\mathbf{p}) = \nabla_{\mathbf{p}} \mathcal{L}(\mathbf{y}(t; \mathbf{p}), \mathbf{p}, \mathbf{z}(t)) = \mathbf{R}^T \mathbf{R}(\mathbf{p} - \mathbf{p}_0) - \int_0^T \nabla_{\mathbf{p}} \mathcal{F}^T \mathbf{z}(t) dt \quad (10)$$

354 and should be equal to zero at optimality. This is equivalent to say that the  
 355 optimal parameters depend on a weighted time average of the derivative of  
 356 the state equation (3) with respect to the parameters vector  $\mathbf{p}$ , multiplied by  
 357 the solution of the adjoint state problem (9).

358 The minimization problem eventually consists in solving three ODEs with  
 359 unknowns  $(\mathbf{y}(t), \mathbf{z}(t), \mathbf{p})$ : the forward problem (3), the adjoint problem (9)  
 360 and the optimality equation (10) set equal to zero. The straightforward  
 361 solution is not possible here, as the adjoint problem is time-backward: a  
 362 staggered process is then proposed instead, where the forward and adjoint  
 363 problems are solved successively on the one hand, and the optimality equation  
 364 on the other hand is used to derive successive estimates of the misfit function  
 365 gradient. These estimates are used in a classical gradient-based optimization  
 366 algorithm, such as a line-search or a trust-region method. In addition, for  
 367 the solution of the adjoint state problem, a change of variable for the time is  
 368 first introduced in order to solve a time-forward problem along with initial  
 369 conditions, rather than the original time-backward problem.

370 In terms of computational cost, evaluating the gradient of the misfit func-  
 371 tion is cheaper and more robust using the adjoint state formulation than with  
 372 a finite difference formula. Whenever evaluating the gradient associated with  
 373  $P$  parameters, the finite difference formula requires the solutions of  $P$  addi-  
 374 tional forward problems, each one being evaluated with the same parameters

375 as the computed forward problem, except for one parameter which is slightly  
 376 perturbed in order to derive the corresponding component of the misfit func-  
 377 tion gradient. In addition, the computation of an integral is required for  
 378 each of these  $P$  forward solutions, in order to evaluate the associated misfit  
 379 function.

380 On the contrary, when using the adjoint state formulation, only one ad-  
 381 ditional ODE (9) has to be solved, and since this ODE is formally close to  
 382 the forward problem, the solution of the adjoint state problem has the same  
 383 cost as the solution of the forward problem. Then the computation of an  
 384 integral is needed for each component of the gradient. To conclude, for each  
 385 step of the staggered process, only two ODEs have to be solved and  $N$  inte-  
 386 grals have to be evaluated when using the adjoint state formulation, whereas  
 387  $P + 1$  ODE solutions and  $N$  integrals evaluations are required with the finite  
 388 difference formula.

## 389 5. Parameter identification of the RT model

### 390 5.1. Formulation of the identification problem

391 The parameter identification is achieved according to the formulation pre-  
 392 sented in the previous section. Similarly to (4), the misfit function quantifies  
 393 the discrepancy between the computed and measured forces when a specific  
 394 displacement is prescribed to the bushing:

$$\begin{aligned} \mathcal{J}(\mathbf{p}) &= \frac{1}{2} \int_0^T |K_0 y_0(t) + K_{pa}(y_0(t) - y_1(t; \mathbf{p})) - F_{exp}(t)|^2 dt \quad (11) \\ &+ \frac{1}{2} |\mathbf{R}(\mathbf{p} - \mathbf{p}_0)|^2 \end{aligned}$$

395 where  $F_{exp}(t)$  is the measured force,  $\mathbf{R} = \text{diag}(R_{K_0}, R_{K_{pa}}, R_{K_r}, R_{C_0}, R_\alpha)$  com-  
 396 prises the different regularization parameters to be set, and typical values for  
 397 the different parameters are in  $\mathbf{p}_0 = (K_0^0 \ K_{pa}^0 \ K_r^0 \ C_0^0 \ \alpha^0)^\top$ .

398 The adjoint state formulation used for evaluating the misfit function gra-  
 399 dient consists in solving the following time-backward equations:

$$\begin{aligned} &(K_{pa} + K_r)z_1(t) - K_r z_2(t) - C_0 \alpha |y_1'(t; \mathbf{p})|^{\alpha-1} z_1'(t) \quad (12) \\ &- C_0 \alpha (\alpha - 1) \text{sign}(y_1'(t; \mathbf{p})) y_1''(t; \mathbf{p}) |y_1'(t; \mathbf{p})|^{\alpha-2} z_1(t) = -K_{pa}(F(t; \mathbf{p}) - F_{exp}(t)) \\ &\quad \vdots \\ &-K_r z_{k-1}(t) + 2K_r z_k(t) - K_r z_{k+1}(t) - C_0 \alpha |y_k'(t; \mathbf{p})|^{\alpha-1} z_k'(t) \end{aligned}$$



416 in the equations to solve, with errors of a magnitude independent of the time  
 417 step size. The authors then propose to smooth the discontinuities, and show  
 418 that the correct gradient values can be evaluated when the time step size is  
 419 'sufficiently small' in comparison with the smoothing parameter.

420 Therefore, in order to smooth the solved equations, we replaced the occur-  
 421 rences of the sign and absolute value functions by the following expressions  
 422 respectively:

$$\begin{aligned} \text{sign}_s(y') &= \frac{2}{1 + e^{-sy'}} - 1 \\ |y'|_s &= \frac{2}{s} \ln \left( 1 + e^{sy'} \right) - y' \end{aligned} \quad (14)$$

423 where  $s$  is a constant to set: the lower  $s$  is, the smoother the functions  $\text{sign}_s$   
 424 and  $|\cdot|_s$  are. The first function is actually a classical sigmoid function, and  
 425 the second one is the primitive function of the first one: this allows to directly  
 426 replace the sign and absolute value functions by their smoothed counterparts  
 427 in Equations (2), (12) and (13). The influence of the smoothing parameter  
 428  $s$  is depicted in Figure 10. To determine the best value for  $s$ , the accuracy  
 429 of the adjoint state solution has to be determined.

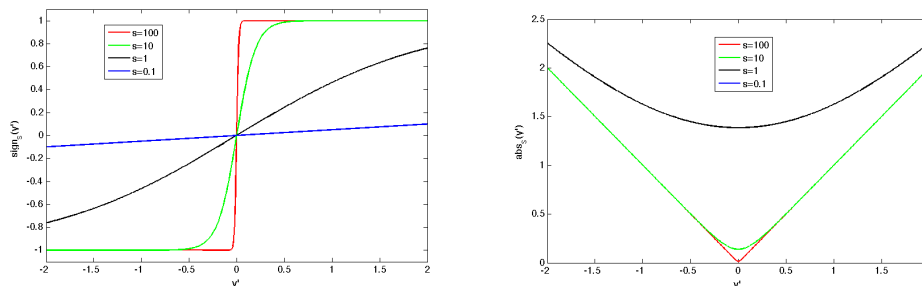


Figure 10: Influence of the smoothing parameter  $s$ : smoothed sign function (left) and smoothed absolute value function (right)

### 430 5.2. Validation of the adjoint state solution

431 A classical way to check the accuracy of the computed adjoint state is  
 432 to use the mathematical property of the adjoint state equation (9), whose

433 operator  $\mathcal{G}$  should be the adjoint of the operator associated with the dif-  
 434 ferentiated forward state equation  $\nabla_{\mathbf{y}}\mathcal{F}$ . The idea is to solve the following  
 435 equations, for any arbitrary vector  $\mathbf{a}$ :

$$\begin{aligned}\nabla_{\mathbf{y}}\mathcal{F} \mathbf{b} &= \mathbf{a} \\ \mathcal{G} \mathbf{c} &= \mathbf{b}\end{aligned}\tag{15}$$

436 Since theoretically one has  $\nabla_{\mathbf{y}}\mathcal{F}^T = \mathcal{G}$ , the following equality should hold,  
 437 provided the adjoint state has been correctly solved:

$$\mathbf{a}^T \mathbf{c} = \mathbf{b}^T \mathbf{b}\tag{16}$$

438 This dot-product test should be verified for different values of  $\mathbf{a}$  to be posi-  
 439 tively sure that the adjoint state solution is correctly calculated.

440 A series of numerical tests were conducted in order to determine the most  
 441 relevant value that should be chosen for the smoothing parameter  $s$ . Using  
 442 an arbitrary set of parameter values  $\mathbf{p}_{exp} = (K_0^{exp} K_{pa}^{exp} K_r^{exp} C_0^{exp} \alpha^{exp})^T$   
 443 in Equation (2) to simulate an experimental reference, the misfit function  
 444 (with no regularization term) and its gradient are evaluated for a given set  
 445 of parameters whose values are quite different from the experimental ones:  
 446  $(K_0^{exp}/2 \ 2K_{pa}^{exp} \ K_r^{exp}/2 \ C_0^{exp}/2 \ 2\alpha^{exp})^T$ . The results in the case of different  
 447 values of  $s$  (as well as without any smoothing) are listed in Table 1. In  
 448 addition, the dot-product test (16) has been applied for  $\mathbf{a} = (1 \ \dots \ 1)^T$  and  
 449 the associated results are listed in Table 1 as well.

Smoothing	$\mathcal{J}$	$\nabla_{K_0}\mathcal{J}$	$\nabla_{K_{pa}}\mathcal{J}$	$\nabla_{K_r}\mathcal{J}$	$\nabla_{C_0}\mathcal{J}$	$\nabla_{\alpha}\mathcal{J}$	$\mathbf{a}^T \mathbf{c}$	$\mathbf{b}^T \mathbf{b}$
$s = 0.1$	921 787.149	-4 752.446	-16.3299	-277.728	49 467.59	-13 149.70	0.021 569	0.021 576
$s = 1$	888 192.640	-4 665.399	-17.630	-268.873	67 022.15	-13 154.49	0.021 378	0.021 351
$s = 10$	888 192.739	-4 665.399	-17.735	-285.087	38 570.69	-11 927.34	0.028 785	0.020 740
$s = 100$	888 192.736	-4 665.399	$-5.6 \cdot 10^9$	$-8.2 \cdot 10^9$	$-1.3 \cdot 10^{13}$	$1.2 \cdot 10^{12}$	$> 3 \cdot 10^7$	0.020 359
none	888 192.736	-4 665.399	infinite	infinite	infinite	infinite	infinite	0.020 245

Table 1: Evaluation of the misfit function and its gradient, and dot-product test for different smoothing settings

450 As predicted, the dot-product test is more and more accurately verified  
 451 as the smoothing increases, that is as  $s$  decreases. Other values of  $\mathbf{a}$  give  
 452 similar results. The best value for the smoothing seems to be  $s = 1$ , for it  
 453 represents a trade-off between the correct estimation of the misfit function  
 454  $\mathcal{J}$  (and of its gradient) and the validation of the adjoint state characterized  
 455 by the dot-product test.

456 In Table 2, we compare the directional derivatives previously computed  
457 with  $s = 1$  with those estimated with a finite-difference formula and no  
458 smoothing. Even if the estimates are of the same order of magnitude, some  
459 differences can be noticed, excepted for  $\nabla_{K_0}\mathcal{J}$  where  $\mathbf{z}$  is not used. On  
460 the one hand, the computed problems are slightly different because of the  
461 smoothing; on the other hand, the estimates which are computed using a  
462 finite-difference formula without smoothing can not be considered as refer-  
463 ences, for they depend on the discretisation step used in the formula and  
464 the smaller this discretisation step, the stronger the impact of the tolerance  
465 of the forward state solution on the result of the formula. All in all, using  
466 some smoothing and estimating the misfit function gradient by means of the  
467 adjoint state seems to be relevant to solve the identification problem, as can  
468 be seen in the following section. Eventually, the value  $s = 1$  is used in what  
469 follows.

Method	$\nabla_{K_0}\mathcal{J}$	$\nabla_{K_{pa}}\mathcal{J}$	$\nabla_{K_r}\mathcal{J}$	$\nabla_{C_0}\mathcal{J}$	$\nabla_{\alpha}\mathcal{J}$
adjoint state with smoothing	-4 665.399	-17.630	-268.873	67 022.15	-13 154.49
finite diff. without smoothing	-4 665.399	-6.7776	-241.145	39 672.53	-8 141.242

Table 2: Evaluation of the misfit function gradient

### 470 5.3. Identification results with synthetic data

471 In order to assess the accuracy of the identification process, preliminary  
472 tests using synthetic data are proposed. Since actual experimental data come  
473 from imposed quasistatic periodic inputs as well as Heaviside step functions,  
474 it seems relevant to study similar inputs to quantify the accuracy of the  
475 identification results. The final choice here is to compute the response to  
476 sinusoidal displacements, and use them as synthetic data for the identification  
477 process. Figure 6 (left) shows the typical curves that can be obtained for such  
478 inputs. Synthetic data are computed using an arbitrary set of parameter  
479 values  $\mathbf{p}_{exp} = (K_0^{exp} K_{pa}^{exp} K_r^{exp} C_0^{exp} \alpha^{exp})^T$  in the forward problem (2), for  
480 a sinusoidal displacement input of 1Hz-frequency.

481 Two different gradient-based algorithms, proposed in the Optimisation  
482 Toolbox for Matlab, are tested: a line-search method, consisting in a Quasi-  
483 Newton method with the BFGS formula for the approximation of the Hessian  
484 matrix [17], and a trust-region method, based on the interior reflective New-  
485 ton method [19]. Identification results for both methods and close initial

486 values  $(K_0^{exp} \ 4K_{pa}^{exp}/3 \ 2K_r^{exp}/3 \ 2C_0^{exp} \ 2\alpha^{exp})^T$  are listed in Table 3. They  
 487 range from satisfactory to excellent depending on the parameter, and tend  
 488 to be better with the trust-region method.

Method	$\frac{K_0}{K_0^{exp}}$	$\frac{K_{pa}}{K_{pa}^{exp}}$	$\frac{K_r}{K_r^{exp}}$	$\frac{C_0}{C_0^{exp}}$	$\frac{\alpha}{\alpha^{exp}}$
line-search	1.099	1.095	0.649	0.972	1.524
trust-region	1.001	0.975	0.767	1.270	0.922

Table 3: Identification results for synthetic data and initial values close to the 'experimental' ones

489 In order to check the robustness of the identification process, initial values  
 490 much farther from the values used for computing the synthetic data are  
 491 proposed:  $(2K_0^{exp} \ 5K_{pa}^{exp} \ K_r^{exp}/5 \ C_0^{exp}/5 \ 5\alpha^{exp})^T$ . They lead to the results  
 492 listed in Table 4. The results are far worse than in the case of initial values  
 493 chosen close to the 'experimental' ones. This means that there are many local  
 494 minima in the misfit function, making the identification process difficult as  
 495 is. In addition, some parameters, such as  $C_0$  and  $\alpha$ , seem not to have a  
 496 strong impact on the response, for the bushing is loaded in a quasi-static  
 497 way. Despite this final remark, it can be concluded that, between the two  
 498 methods, the trust-region method gives the best results.

Method	$\frac{K_0}{K_0^{exp}}$	$\frac{K_{pa}}{K_{pa}^{exp}}$	$\frac{K_r}{K_r^{exp}}$	$\frac{C_0}{C_0^{exp}}$	$\frac{\alpha}{\alpha^{exp}}$
line-search	1.328	5.121	0.227	0.498	7.954
trust-region	1.300	2.960	0.361	0.499	4.884

Table 4: Identification results for synthetic data and initial values far from the 'experimental' ones

499 To go further, some regularization is then required. It is not, however,  
 500 straightforward when dealing with the actual experimental data: since the  
 501 model uses rheological elements, there are no typical values which can eas-  
 502 ily be chosen for the vector  $\mathbf{p}_0 = (K_0^0 \ K_{pa}^0 \ K_r^0 \ C_0^0 \ \alpha^0)^T$ . Moreover, there is  
 503 actually no quantitative information available concerning the measurement  
 504 noise corrupting the experimental data. Applying principles such as Moro-  
 505 zov's [20] in order to set relevant values for the regularization parameters  
 506 contained in  $\mathbf{R}$  is then not really possible. With these two drawbacks, the

507 resulting regularization may not be relevant; therefore, rather than applying  
 508 a classical Tikhonov's regularization in the identification process, a technique  
 509 is proposed in the following section to give a first guess of the initial values  
 510 to be used in the minimization algorithm.

#### 511 5.4. Determination of relevant initial values for the identification process

512 Due to the ill-posedness of the identification problem, it is crucial to  
 513 be able to give relevant initial values to the minimization algorithm in or-  
 514 der not to converge to a local minimum which would lie too far from the  
 515 global one. This can be done by using the STS model described in Sec-  
 516 tion 3.1 rather than the RT model, because the STS model can be analyti-  
 517 cally inverted under some simple assumptions. Starting from the experimen-  
 518 tal hysteresis curve, it is possible to get values for the associated parameters  
 519  $\mathbf{p}_{STS} = (K_0^S \ K_{pa}^S \ K_r^S \ F_f)^T$ . Then, initial values for the RT model's param-  
 520 eters can be derived from these parameter values.

521 First, it is assumed that all the STS cells but one (*i.e.*  $N - 1$  cells) are  
 522 loaded when the hysteresis curve is obtained: this is equivalent to assume that  
 523 the bushing is loaded with a sufficiently high-amplitude displacement. In this  
 524 case, three representative features of the hysteresis curve can be determined  
 525 as functions of the STS parameters  $\mathbf{p}_{STS} = (K_0^S \ K_{pa}^S \ K_r^S \ F_f)^T$ :

- 526 • the secant stiffness associated with the two extremities of the hysteresis  
 527 cycle (with  $N$  odd):

$$K_{\text{sec}} = K_0^S + \frac{K_{pa}^S K_r^S}{\frac{N-1}{2} K_{pa}^S + K_r^S} \quad (17)$$

- 528 • the slope of the line being tangent to the hysteresis cycle just after a  
 529 cusp:

$$T_{g1} = K_0^S + K_{pa}^S \quad (18)$$

- 530 • the slope of the line being tangent to the hysteresis cycle just before a  
 531 cusp:

$$T_{g2} = K_0^S + \frac{K_{pa}^S K_r^S}{(N-1)K_{pa}^S + K_r^S} \quad (19)$$

532 These features are summarized on Figure 11. Finally, the maximal force  $F_{\max}$   
 533 applied on the bushing when  $N - 1$  STS cells are loaded can be written as  
 534 follows:

$$F_{\max} = K_0 \left( \frac{F_f N(N-1)}{K_r^S} + \frac{2F_f N}{K_{pa}^S} \right) + 2NF_f \quad (20)$$

535 This maximal force is obtained for a displacement amplitude  $X_{\max}$ , which  
 536 means that  $F_{\max} = K_{\text{sec}} X_{\max}$ .

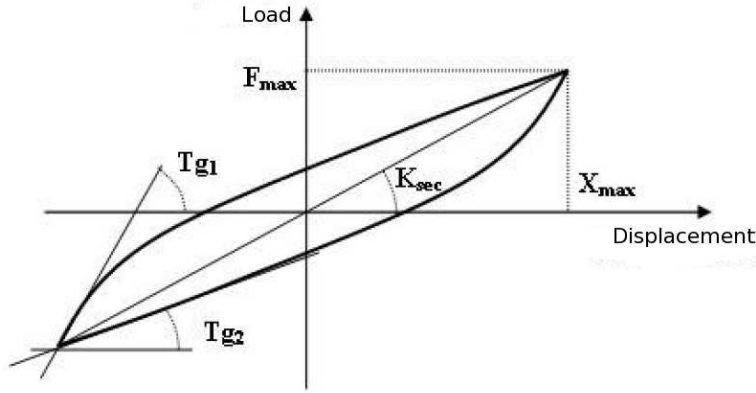


Figure 11: Features of the hysteresis curve associated with the STS model

537 The previous formulas can be reversed in order to determine the STS  
 538 parameters  $\mathbf{p}_{STS} = (K_0^S \ K_{pa}^S \ K_r^S \ F_f)^T$ , for example in terms of slopes before  
 539 and after a cusp, and maximal force and displacement :

$$K_0^S = \frac{F_{\max}(T_{g1} + T_{g2}) - 2T_{g1}T_{g2}X_{\max}}{2F_{\max} - (T_{g1} + T_{g2})X_{\max}} \quad (21)$$

$$K_{pa}^S = \frac{(T_{g1} - T_{g2})(F_{\max} - T_{g1}X_{\max})}{2F_{\max} - (T_{g1} + T_{g2})X_{\max}} \quad (22)$$

$$K_r^S = -\frac{(N-1)(T_{g1} - T_{g2})(F_{\max} - T_{g1}X_{\max})(F_{\max} - T_{g2}X_{\max})}{(2F_{\max} - (T_{g1} + T_{g2})X_{\max})^2} \quad (23)$$

$$F_f = \frac{(F_{\max} - T_{g1}X_{\max})(F_{\max} - T_{g2}X_{\max})}{N(2F_{\max} - (T_{g1} + T_{g2})X_{\max})} \quad (24)$$

540 If it is assumed that the STS and RT models are roughly similar, the first  
 541 three expressions can give straightforward initial values for the first three RT

542 model's parameters:

$$K_0^0 = K_0^S \quad K_{pa}^0 = K_{pa}^S \quad K_r^0 = K_r^S \quad (25)$$

543 In order to determine estimates for the last two, it is assumed that the  
 544 viscoelastic part (1) of the RT cell should be analogous to the threshold  
 545 force  $F_f$  of the STS cell when the bushing is loaded at a (mean) speed  $V_0$ ,  
 546 that is:

$$C_0^0 = \frac{F_f}{V_0^{\alpha^0}} \quad (26)$$

547 To remain quite close to the solid friction behaviour of the STS cell, an  
 548 arbitrary choice of a small value for  $\alpha^0$  is made, such as one tenth or one  
 549 fifth.

550 This strategy has been tested on the example from the previous section.  
 551 In Table 5 are listed the initial values of the RT model's parameters that  
 552 are obtained from the synthetic hysteresis cycle when two different values  
 553 of  $\alpha^0$  are proposed. The obtained values show some discrepancies with the  
 554 'experimental' ones: it can be explained by the fact that the slopes  $T_{g1}$  and  
 555  $T_{g2}$  cannot be determined without some error and that any inaccuracy in the  
 556 associated values can have a strong impact on the determination of the STS  
 557 model's parameter values. As an example of this sensitivity, Figure 12 shows  
 558 how the first three STS model's parameters evolve as the measured value of  
 559 the slope  $T_{g2}$  varies: the changes can go up to nearly 100% for a 10%-change  
 560 in the value  $T_{g2}$ . As any other inverse problem, the quality of the inversion  
 561 of the formulas associated with the STS model shows a strong dependence  
 562 on the noise in the measurements.

$\alpha^0$	$\frac{K_0^0}{K_0^{exp}}$	$\frac{K_{pa}^0}{K_{pa}^{exp}}$	$\frac{K_r^0}{K_r^{exp}}$	$\frac{C_0^0}{C_0^{exp}}$
1/10	0.770	1.105	1.468	0.703
1/5	0.770	1.105	1.468	0.740

Table 5: Initial RT model's parameter values using an STS model identification and the synthetic hysteresis cycle

563 All these results, however, show that it is possible to get reasonable initial  
 564 values for the RT model's parameters: all the proposed values lie in a range  
 565 of the same magnitude as the one proposed in the first identification exam-  
 566 ple with synthetic data (with associated results in Table 3). Moreover, the

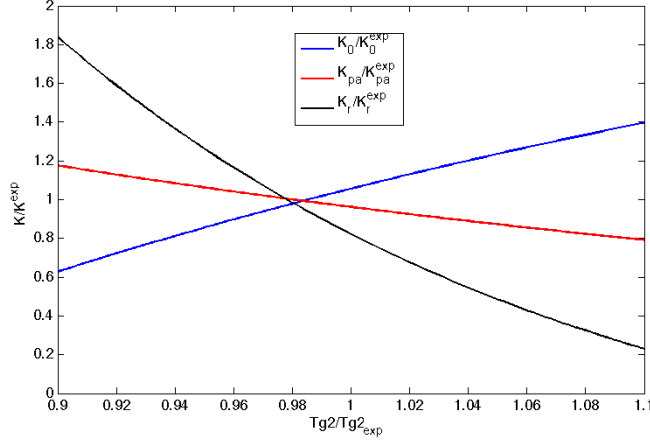


Figure 12: Normalized values of the first three STS model's parameters with respect to the slope  $T_{g2}$  measured on the hysteresis curve

567 arbitrary choice of a value for  $\alpha^0$  does not seem to have too high an impact  
 568 on the proposed value for  $C_0^0$ . Finally, since all these values are perturbed by  
 569 some noise, it seems better, as stated previously, to use them as initial values  
 570 for the minimization algorithm rather than nominal values in a Tikhonov's  
 571 regularization term such as the one proposed in (11). The resulting benefit  
 572 should be the minimization algorithm to likely start in the attraction basin  
 573 of the global minimum of the misfit function.

#### 574 5.5. Identification results from actual data

575 As described previously, actual experimental data come from quasistatic  
 576 periodic as well as fast transitory loads, applied to the bushing by means of  
 577 a specific test rig. Two simple test configurations are proposed: the first one  
 578 consists in applying to the bushing a triangular periodic displacement at a  
 579 rather limited speed and is used in the identification process. The second  
 580 configuration consists in applying a displacement characterised by a Heav-  
 581 iside step function to observe relaxation in the bushing (the input being  
 582 not truly discontinuous, but being characterised by a 0.1s time interval of  
 583 increase): but rather than using the associated measurements in the iden-  
 584 tification process as well, one prefers to keep them as a further reference in  
 585 order to validate the identified model *a posteriori*.

586 The same gradient-based algorithms as in Section 5.3 are used here. Ini-  
587 tial values of the RT model’s parameters are given according to the strategy  
588 described in Section 5.4; since the experimental curve (depicted in Figure 13  
589 or 14) is not perfectly symmetric, an average value of each feature has been  
590 used. Table 6 lists the (relative) identified values of the RT model’s param-  
591 eters as well as a normalized value of the discrepancy between the model’s  
592 results and experimental data: this value is calculated as the square root  
593 of the final misfit function divided by a norm  $\mathcal{J}_0$  of the experimental data,  
594 defined by the following expression:

$$\mathcal{J}_0 = \frac{1}{2} \int_0^T |F_{exp}(t)|^2 dt \quad (27)$$

595 This normalized value is a good guess of the relative identification error.  
596 Whereas this error was equal to 15.32% with the proposed initial values, it  
597 drops significantly for the values identified with the two methods. Eventually,  
598 the two methods lead to very similar results, even if the line-search method  
599 seems to provide a slightly better solution.

Method	$\frac{K_0}{K_0^0}$	$\frac{K_{pa}}{K_{pa}^0}$	$\frac{K_r}{K_r^0}$	$\frac{C_0}{C_0^0}$	$\frac{\alpha}{\alpha^0}$	$\sqrt{\frac{\mathcal{J}}{\mathcal{J}_0}}$
line-search	1.217	1.049	1.088	0.930	1.197	3.11%
trust-region	1.182	1.145	1.156	0.889	1.153	3.20%

Table 6: Identification results for actual data (triangular periodic displacement)

600 Figures 13 and 14 (left) show for each method the comparison between  
601 the experimental data and the responses associated with the initial RT model  
602 and with the identified RT model. As seen previously with the relative  
603 errors, the agreement is very good in the case of the triangular periodic  
604 loading. Let us note that only the stabilised hysteresis curves are recorded  
605 in these quasistatic tests: no information is available on the first loading  
606 of the bushing. This latter is mandatory in the numerical simulation: it  
607 is introduced by considering that a linearly-varying displacement is applied  
608 to the bushing: afterwards, the stabilised hysteresis cycle is obtained. The  
609 misfit function is based on these experimental and predicted stabilised cycles  
610 only.

611 Validation of these results is possible with the experimental response to  
612 the Heaviside step function, which has not been used in the identification

613 process. Figures 13 and 14 (right) show the good agreement between the  
 614 response associated with the identified RT model and the experimental data.  
 615 Since these latter have not been used in the identification process, this result  
 616 shows the relevance of the RT model as well as the quality of the identification  
 617 of the associated parameters. In particular, both the relaxation phenomenon  
 618 and the asymptotic steady-state load are well described by the identified  
 619 model, when compared with the experimental data.

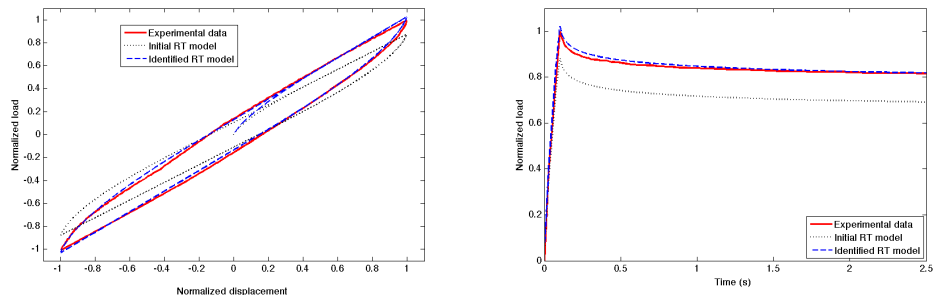


Figure 13: Identification results with the line-search method: comparison with the experimental data used (left) and with experimental data not used in the identification process (right)

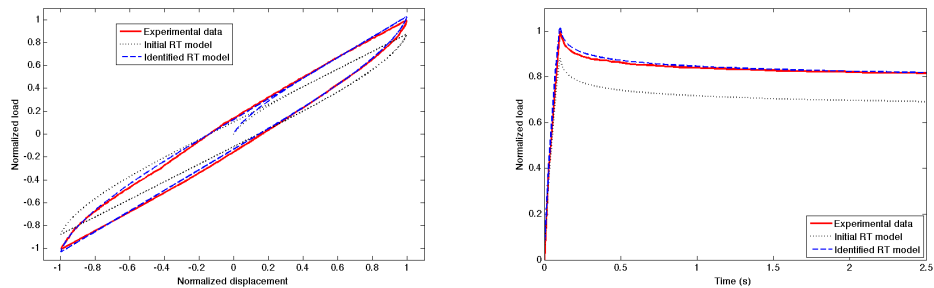


Figure 14: Identification results with the trust-region method: comparison with the experimental data used (left) and with experimental data not used in the identification process (right)

## 620 **6. Conclusion**

621 Here a strategy for identifying the parameters of a nonlinear time-dependent  
622 model has been presented and applied on the example of a rubber bushing  
623 typically used in car chassis. The proposed model is based on components  
624 exhibiting a viscoelastic behaviour which can tend towards the description  
625 of contact-type phenomena. The identification has been achieved in the time  
626 domain using an adjoint state formulation allowing an efficient estimation of  
627 the misfit function's gradient.

628 It was shown that the near-discontinuous behaviour of the proposed model  
629 can lead to numerical difficulties, which may prevent the model's parameters  
630 to be correctly identified due to an inaccurate estimation of the adjoint state  
631 variable. The solution has consisted in smoothing the discontinuities by  
632 means of sigmoid functions: a trade-off allowed to correct the estimates of  
633 the adjoint state without any significant loss of accuracy for the forward state  
634 solution.

635 The relevance of the proposed model as well as the robustness of the  
636 method have been shown with the parameter identification from actual data:  
637 in addition, the obtained results have been validated with experimental in-  
638 formation which was not used in the identification process. Such an iden-  
639 tification allows to deal with accurate models, which are simple enough to  
640 be implemented in multibody simulation softwares, allowing to study well-  
641 known phenomena occurring in a typical vehicle chassis.

642 In a more general way, the strategy presented here can be applied to other  
643 time-dependent problems with contact-type phenomena, and should allow to  
644 achieve the parameter identification both accurately and efficiently.

## 645 **7. Acknowledgements**

646 The authors would like to acknowledge the support of PSA Peugeot  
647 Citroën for this study.

## 648 **References**

- 649 [1] A. Lion, A constitutive model for carbon black filled rubber: experimen-  
650 tal investigations and mathematical representation, *Continuum Mechan-*  
651 *ics and Thermodynamics* 6 (1996) 153–169.

- 652 [2] C. Miehe, J. Keck, Superimposed finite elastic-viscoelastic-plastoelastic  
653 stress response with damage in filled rubbery polymers. Experiments,  
654 modelling and algorithmic implementation, *Journal of the Mechanics  
655 and Physics of Solids* 48 (2000) 323–365.
- 656 [3] P. Haupt, K. Sedlan, Viscoplasticity of elastomeric materials: experi-  
657 mental facts and constitutive modelling, *Archive of Applied Mechanics*  
658 71 (2001) 89–109.
- 659 [4] A. R. Payne, A note on the existence of a yield point in the dynamic  
660 modulus of loaded vulcanizates, *Journal of Applied Polymer Science*  
661 3 (7) (1960) 127.
- 662 [5] L. Mullins, Softening of rubber by deformation, *Rubber Chemistry and  
663 Technology Journal* 42 (1969) 339–362.
- 664 [6] V. A. Coveney, D. E. Johnson, D. M. Turner, A triboelastic model for  
665 the cyclic mechanical behavior of filled vulcanizates, *Rubber Chemistry  
666 and Technology Journal* 68 (1995) 660–670.
- 667 [7] V. A. Coveney, D. E. Johnson, D. M. Turner, Rate-dependent modeling  
668 of a highly filled vulcanizate, *Rubber Chemistry and Technology Journal*  
669 73 (4) (2000) 565–577.
- 670 [8] U. Tornar, Application of strain integral damping to engine mounts, in:  
671 P. Sas, M. De Mucnck (Eds.), *ISMA 2006 - International Conference  
672 on Noise and Vibration Engineering*, Leuven, Belgium, 2006, pp. CD-  
673 ROM.
- 674 [9] R. L. Bagley, P. J. Torvik, Fractional calculus - a different approach  
675 to the analysis of viscoelastically damped structures, *AIAA Journal* 21  
676 (1983) 741–748.
- 677 [10] M. Sjöberg, L. Kari, Nonlinear isolator dynamics at finite deforma-  
678 tions: an effective hyperelastic, fractional derivative, generalized friction  
679 model, *Nonlinear Dynamics* 33 (2003) 323–336.
- 680 [11] J.-F. Deü, D. Matignon, Simulation of fractionally damped mechani-  
681 cal systems by means of a Newmark-diffusive scheme, *Computers and  
682 Mathematics with Applications* 59 (2010) 1745–1753.

- 683 [12] R. Bouc, Modèle mathématique d'hystérésis, *Acustica* 24 (1971) 16–25.
- 684 [13] Y. K. Wen, Method of random vibration of hysteretic systems, *ASCE*  
685 *Journal of the Engineering Mechanics Division* 102 (1976) 249–263.
- 686 [14] Y. Q. Ni, J. M. Ko, C. W. Wong, Identification of non-linear hysteretic  
687 isolators from periodic vibration tests, *Journal of Sound and Vibration*  
688 217 (4) (1998) 737–756.
- 689 [15] J. K. Ok, W. S. Yoo, J. H. Sohn, New nonlinear bushing model for gen-  
690 eral excitations using Bouc-Wen hysteretic model, *International Journal*  
691 *of Automotive Technology* 9 (2) (2008) 183–190.
- 692 [16] A. Constantinescu, N. Tardieu, On the identification of elastoviscoplastic  
693 constitutive laws from indentation tests, *Inverse Problems in Science and*  
694 *Engineering* 9 (1) (2001) 19–44.
- 695 [17] J. Nocedal, S. J. Wright, *Numerical Optimization*, 2nd Edition,  
696 Springer, 2006.
- 697 [18] D. E. Stewart, M. Anitescu, Optimal control of systems with discon-  
698 tinuous differential equations, *Numerische Mathematik* 114 (4) (2010)  
699 653–695.
- 700 [19] T. F. Coleman, Y. Li, On the convergence of reflective Newton methods  
701 for large-scale nonlinear minimization subject to bounds, *Mathematical*  
702 *Programming* 67 (2) (1994) 189–224.
- 703 [20] V. A. Morozov, *Methods for solving incorrectly posed problems*,  
704 Springer, 1984.